

Tech Report II (2022) - MagRes Project

Tough epoxy resin systems for cryogenic applications

Publication in preparation - current data not yet published

Pascal Studer^a, Alain Schwegler^a, Theo A. Tervoort^{a,*}

^a*Department of Materials, ETH Zurich, Vladimir-Prelog-Weg
5, 8093 Zurich, Switzerland*

Abstract

In this work, epoxy resins containing different amounts and types of alkylamines, acting as chain extenders in the epoxy network, were produced and characterized mechanically. The use of *flexible* aliphatic amine chain extenders resulted in significantly improved cryogenic fracture toughness of $5.3 \text{ MPa}\sqrt{\text{m}}$ at 77 K for the best system, which is in contrast to the base system, or systems containing rigid aliphatic chain extenders. The improvements in toughness could not be attributed to the occurrence of nanophase separation since x-ray diffraction studies and dynamic mechanical measurements did not reveal such nanoscale phase separation. When sterically hindered alkylamine (2-heptylamine) was used as a chain extender, the processable lifetime increased more than twofold and results in resin formulations with very long processing lifetime. Additionally, we synthesized another chain extender having a lower volatility than the other alkylamines, thus obtaining a component that could be used in vacuum infiltration processes.

*Corresponding author

Email address: `tervoort@ethz.ch` (Theo A. Tervoort)

However, the chemical and network structure of resins using this hardener has yet to be optimized.

Keywords: Epoxy resins, Nanophase separation, fracture toughness, cryogenic

1. Introduction

Epoxy thermoset systems are the material of choice for the encapsulation of superconducting coils for high and low-temperature superconductive magnets. For this application, a number of boundary conditions must be fulfilled [1]. These include, firstly, the requirement that the epoxy must have a high modulus and strength at room temperature to protect and support the superconducting coils, especially during assembly of the magnet. Secondly, after mixing the reactive components, the epoxy system must have a low viscosity and a slow curing reaction, often denoted as having a long “pot-life”, to allow for complete infiltration of the superconducting coils. Finally the epoxy should be resistant against radiation and have a high fracture toughness at cryogenic temperatures to reduce mechanically induced thermal events as those that accompany plastic yielding and crack growth, and which result in the need to excessive training of the magnet.

This research focuses on formulating epoxy compositions that combine a low viscosity and a long pot-life with good mechanical properties at room temperature and cryogenic (liquid nitrogen) temperatures. The condition of good mechanical properties at room temperature requires the glass transition temperature (T_g) of the epoxy to be above room temperature. It should, however, not be too high, to prevent the accumulation of thermal stress dur-

ing cooling. For amorphous thermoplastics and thermosets (such as epoxies), far below T_g , both the Youngs' modulus and the yield stress depend on the inter -and intramolecular van der Waals interactions, and thus converge to similar values [2].

However, the requirement for epoxies of having a high fracture toughness at cryogenic temperatures is more difficult to realise. Many approaches to improve the fracture resistance of epoxy resins in general have been reported in literature and they can typically be subdivided into two broad classes: extrinsic and intrinsic toughening mechanisms. Extrinsic toughening mechanisms rely on a second phase to improve the toughness of the resulting composite and also strongly affect other mechanical properties such as the elastic modulus [3]. Examples of this approach include the addition of nanoparticles or nanorods [4–7], fibers [8–12], rubber phases [13, 14] or thermoplastics [15]. Approaches towards intrinsic mechanisms of epoxy toughening typically rely on tuning the topology and chemical properties of the covalent network itself instead of introducing a second phase. Examples of intrinsic toughening mechanisms include double networks [16], rearrangement of network topology by solvent encapsulation [17], anionic ring-opening polymerization of epoxy groups [18], addition of reactive diluents [19] or modifications of crosslink density and crosslink point functionality [20, 21].

For applications at cryogenic temperatures, such as the use of epoxies as matrix material in superconducting coils, approaches relying on the ductility of a second phase, such as rubber toughening, fail due to the glassy behaviour of the second phases at cryogenic temperatures. Other extrinsic toughening mechanisms, such as the addition of hard ceramic nanoparticles

or nanorods, rely on the localized yielding of soft polymer matrix around the particles. The question whether these toughening mechanisms can also be extrapolated to cryogenic temperatures is not yet sufficiently answered, with some contradictory results reported in literature [5, 7].

A more recent intrinsic approach for modifying the network topology of a polymer was introduced by Beiner and Huth [22] and consists of introducing olefinic side-chains of different lengths in a poly(n-alkyl acrylate) backbone. Hiller et al. [23] provided conclusive evidence for the existence of phase separation on the nanoscale by the olefinic side-chains. In the epoxy field, research on phase-separating antiplasticizers revealed that the fracture toughness can be significantly improved, even to lower temperatures, when the chemical compatibility of the antiplasticizer is tuned such that it is less compatible with the matrix and occupies spaces between the polymer backbone [24]. Olefinic side-chains in epoxy resins were already employed by Huang et al. [25], who observed phase separation on the microscale by AFM along with improvements of elastic modulus and strain at break. However, they used a stoichiometric excess of amine, and thus some unreacted alkylamines may have formed microphase separation instead of nanophase separation. Based on all these results, we want to investigate the effect of olefinic side-chains in an stoichiometric epoxy network on the toughness at room- and cryogenic temperature. Furthermore, we tried to determine whether nanophase separation can be observed in these resins. The epoxy monomers will be carefully selected for having a low viscosity and a slow curing reaction (long pot-life) in order to satisfy the processing requirements. In addition, a specific alkylamine with a chemical structure expected to provide ideal process-

ing lifetime, low vapour pressure and high toughness, was synthesized by a Williamson ether synthesis and is discussed in the results.

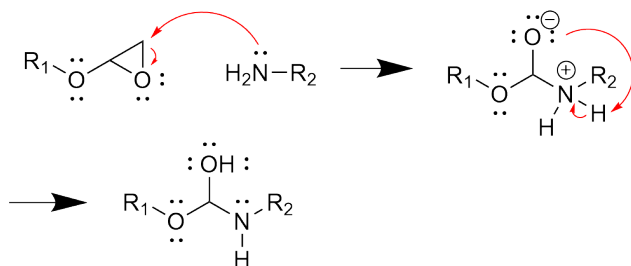


Figure 1: Schematical drawing of the reaction mechanism between an amine group and an epoxy group resulting in the formation of a chain of covalent bonds between R1 and R2.

Since the reaction of an amine group with an epoxide group involves the nucleophilic attack of the amine on the positively charged carbon atom of the epoxide group (see figure 1), introducing sterical hindrance of the amine group should result in a slower reaction speed and increased pot-life [26]. Therefore, in this work, we employed alkylamines with one or two methyl substituents in β -position from the nitrogen atom, to investigate the effect on the reactivity and the pot-life.

2. Experimental

Materials. High purity (> 99 %) chemicals were purchased from Sigma Aldrich and were used without further purification. The chemicals are listed in table 1. Their chemical structures can be seen in figure 2.

Preparation Procedure. In a typical preparation procedure for epoxy samples, the DGEBA component was weighed into a 250 mL round bottom flask and heated to 75 °C in an oil bath equipped with a magnetic stirrer. The DGEBA

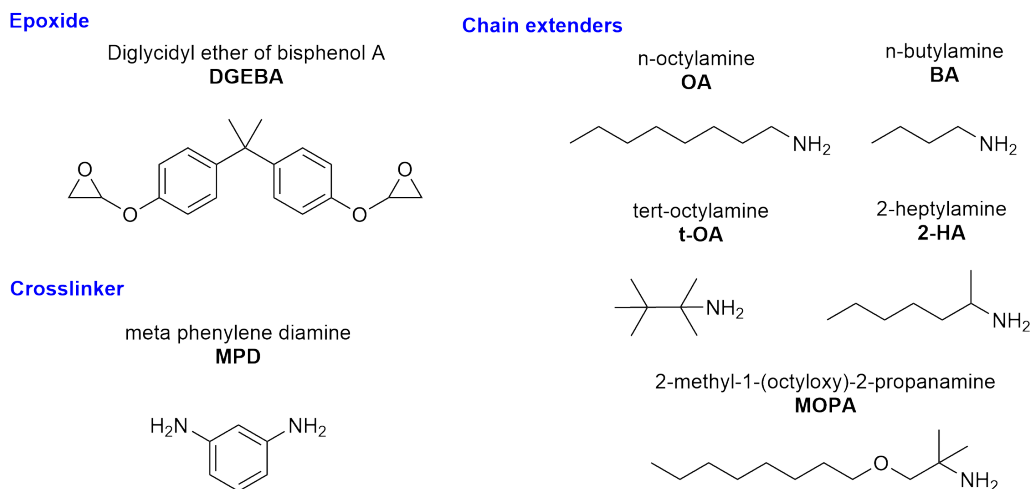


Figure 2: Structure formulas of the different precursor material used in this work to synthesize epoxy resins. DGEBA is the difunctional epoxy monomer, whereas the different alkylamines are also difunctional but belong to the class of amines. The reaction of DGEBA with alkylamines results in linear chains. MPD was used as a crosslinking agent.

was subsequently degassed at 1 mbar for at least 30 min until bubbles evolved infrequently. Subsequently, the appropriate amount of MPD was added to the mixture and dissolved under stirring action while degassing again carefully down to 1 mbar for 10 min. After this, the mixture was removed from the heat, the alkylamine component was added and stirred until the mixture was clear and homogenous. The mixture was then shortly degassed only at 100 mbar due to the potential volatility of some alkylamines. This mixture was then poured into a mold preheated to 100 °C. The mold was then transferred into an oven preheated to 165 °C for curing of the epoxy for 1 hour and 30 minutes. The mold consisted of two aluminium plates coated with PTFE-foil on the inside, separated by a silicone frame and distance holders, and held together by four screw clamps. After cure completion, the mold

Table 1: Monomers used for synthesizing the epoxy resins. F denotes the functionality of the component. EEW/AEW denotes the epoxide or the amine hydrogen equivalent weight, respectively (g/mol).

Name	Abbreviation	F	EEW/AEW (g/mol)
bisphenol A diglycidyl ether	DGEBA	2	172
meta phenylene diamine	MPD	4	27.0
n-octylamine	OA	2	64.6
n-butylamine	BA	2	36.6
tert-octylamine	t-OA	2	64.6
2-heptylamine	2-HA	2	57.6
2-methyl-1-(octyloxy)-2-propanamine	MOPA	2	201.4

was removed from the oven and cooled down in ambient air. All the samples for mechanical testing were produced by water-jet cutting the approximately 5 mm thick epoxy plates into the desired geometries.

Single-edge notch bending tests (SENB). Single edge notch bending tests were performed according to the standard ASTM D-5045 on a Zwick Z020 tensile tester (Zwick Roell, Germany) equipped with a 20 kN load cell using a customized setup. The setup consists of an aluminium tub, which can be filled with liquid nitrogen, supported on a thick PTFE plate for thermal insulation from the bottom post of the tensile tester. A central bottom hole in the aluminium tub allows to place various test geometries. In this case, a two-point support with a spanwidth of $W = 38$ mm was used. The samples had a thickness of $B = 5$ mm and a height of $H = 9.5$ mm. The tests were conducted at a speed of 2 mm/min. For the tests conducted in a liquid

nitrogen bath, the aluminium tub was first cooled down by pouring in liquid nitrogen multiple times. Then the samples were submerged in the liquid nitrogen bath placed correctly on the two-point support in the bath. The test was typically started after waiting for 5 min.

Dynamical mechanical thermal analysis. Dynamic mechanical thermal analysis (DMTA) was performed using a ARES-G2 rheometer (TA instruments, United States) equipped with a three-point bending geometry, forced convection oven and liquid nitrogen supply for cooling. A support span of $W = 40$ mm was used. The sample was placed on the support and held in position by the top geometry using a force of 2 N while the sample was cooled down to -110°C . When the temperature was reached, an oscillatory strain of 0.05 % was applied on the sample at a rate of 1 Hz. The force response of the sample was recorded while the temperatures were ramped at a rate of $2.5^{\circ}\text{C}/\text{min}$ until a temperature well above the glass transition temperature was reached. Rectangular slabs of 3 mm thickness and 5 mm width were used for the tests. The data acquired from DMTA was further used in the determination of the crosslink density, which is described in the paragraph below.

Determination of crosslink density. In Figure 8 it can be seen that the storage modulus E' of all epoxy systems above T_g are to a good approximation linear dependent on temperature. In addition, Figure 8 shows that above T_g , the loss factor $\tan(\delta)$ is small, indicating that in this temperature regime, the epoxies behave to a good approximation as stiff isotropic elastic rubbers. In case of elastic behavior, the storage modulus E' will be approximately equal to the Young's modulus E . Furthermore, as rubbers deform at close

to constant volume, the Poisson's constant ν is approximately $\nu \approx 0.5$, so that for epoxies above T_g , according to Hooke's law, the storage modulus E' is related to the shear modulus G by:

$$E' \approx E = 2G(1 + \nu) \approx 3G \quad (1)$$

According to rubber elasticity theory, the entropic part of the shear modulus G_S of a rubber depends on the molecular weight between crosslinks, M_C , as:

$$G_S = g \frac{\rho RT}{M_c} \quad (2)$$

Here T is the absolute temperature, R is the gas constant, ρ is the polymer density and g is a factor accounting for crosslink mobility, which is assumed to be $g = 1$ for small deformations [27].

However, due to their comparatively high crosslink density, epoxies above T_g cannot be regarded as ideal rubber elastic materials. This follows immediately from extrapolation of E' as a function of temperature above T_g (the linear fits in Fig. 11) to 0 K. According to Eq. 2, all the linear fit lines in Fig. 11 should cross in the origin at 0 K, but this is not what is observed experimentally.

From thermoelasticity of neo-Hookean isotropic materials, it can be shown that the experimentally observed shear modulus G of a material generally consists of an energy elastic contribution G_E and an entropy elastic contribution G_S , where the latter is given by [28]:

$$G_S = T * \frac{\partial G}{\partial T} - \frac{G\alpha T}{3} \quad (3)$$

For epoxies above T_g , the isobaric expansion coefficient α is small ($\alpha \approx 5 \times 10^{-5} \text{ K}^{-1}$ [2]) so that the second term in the right-hand side of this equation can be neglected and G_S can be approximated by:

$$G_S = T * \frac{\partial G}{\partial T} \quad (4)$$

From Eqs. 1, 2 and 4, it then follows that the molar volumetric crosslink density, v , related to M_C as $v = \frac{\rho}{M_C}$, can be determined experimentally above T_g from the slope of E' as a function of T as:

$$v = \frac{1}{R} \left(\frac{\partial G}{\partial T} \right) = \frac{1}{3R} \left(\frac{\partial E'}{\partial T} \right) \quad (5)$$

Prediction of the crosslink density. Because the molecular structures and molar ratios of the used epoxy resin system components are known, predictions of the crosslink density can be made. The bifunctional components of the system, DGEBA and the aliphatic amines, can only act as chain extenders, not increasing the number of elastically active chains in the system. Only MPD can form tri- or tetrafunctional crosslinks. Assuming a perfectly cured network with no dangling chains, each tri- or tetrafunctional MPD molecule contributes 3/2 or 4/2 of elastically active chains, respectively. Since the mass densities of the investigated systems are known, the molar volumetric crosslink density can be estimated using the equation:

$$v = \frac{\rho}{M_{MPD}} \cdot \frac{m_{MPD}}{m_{tot}} \cdot \frac{\bar{f}}{2} \quad (6)$$

Here ρ is the density, M_{MPD} is the molar mass of MPD, m_{MPD} and m_{tot} are the mass of MPD and the total mass of the resin system, respectively, and \bar{f} the average crosslink functionality.

X-ray scattering (SAXS, WAXS). Scattering spectra were recorded using a XEUSS 3.0 x-ray diffractometer (Xenocs, France) on samples with a thickness of approximately 2 mm. The diffractometer is equipped with a copper source generating copper K_α radiation with a wavelength of 1.54 Å, multiple sets of slits for beam collimation, a solid sample holder containing a LaB₆ calibrant for calibration of the sample-detector distance and an Eiger 2R (Dectris, Switzerland) hybrid photon counting detector. The photon counting detector also measures the intensity of the main beam, eliminating the need for an external standard such as glassy carbon to obtain data in absolute intensity units. In order to obtain a wide range of diffraction angles for the USAXS measurements, three measurement series at different sample-detector distances and different slit collimations were performed. The formula for x-ray scattering data in absolute intensity units is given in the following formula:

$$I_{\text{abs}} = \frac{I}{I_0 * T * t * d * \text{sr}} \quad (7)$$

According to formula 7, the absolute intensity equals I , the intensity in counts per second, divided by, I_0 , the incident beam intensity, T , the transmission factor of the sample, t , the measurement time, d , the sample thickness and sr, the solid angle. Background-subtracted data in absolute intensity units were obtained after several correction steps [29]. The background image was subtracted from the sample image, both of which were already normalized by measurement time, solid angle and transmitted intensity ($I_T = I_0 * T$). The so-obtained background corrected data was subsequently normalized by the sample thickness, resulting in absolute intensity

data.

Rheological characterization. Rheological characterization of selected compositions were performed using an MCR-302 rheometer equipped with a peltier cooler (Anton Paar, Austria). A disposable plate-plate aluminium geometry with a diameter of 20 mm was used for the measurements. Oscillatory measurements were performed with the following settings. The gap was 150 μm , the measurement frequency X and the applied strain Y. Since some of the used components, such as the butyl- or heptylamine, are quite volatile, the measurements were performed by obtaining singular measurements of samples taken from a masterbatch at defined points in time.

Tensile Testing. Tensile tests were performed on a Zwick-Z050 tensile tester equipped with a 50 kN load cell, a forced convection oven and hydraulic clamps. Samples approximately 2 mm in thickness and 3.5 mm in width were carefully clamped using the hydraulic clamps in the oven preheated to the desired starting temperature, e.g. 150 $^{\circ}\text{C}$. The clamp separation was pre-set to 40 mm and calibrated to the starting temperature. After applying a preload of 0.1 N to the sample, the test was started and the strain was increased in a strain-rate controlled manner, up to a defined maximum strain. Then, the oven temperature was increased to the next temperature and equilibrated for 5 min after reaching this temperature, before starting the next test. After the tests, the data were converted to stress data by dividing the force by the cross-sectional area of the sample at room temperature, and linear fits of the stress-strain curves were obtained to extract the elastic modulus of each sample at each temperature. For most of the samples, the temperatures of 150, 175, 200 and 225 were used for the measurement, which

is well above the glass transition temperature. However, for the analysis, the temperatures read by a thermocouple close to the samples were used.

Synthesis of a chain extender. A specific chain extender, 2-methyl-1-(octyloxy)-2-propanamine (MOPA), was synthesized by Williamson ether synthesis via an optimized protocol which can be seen in figure 3.

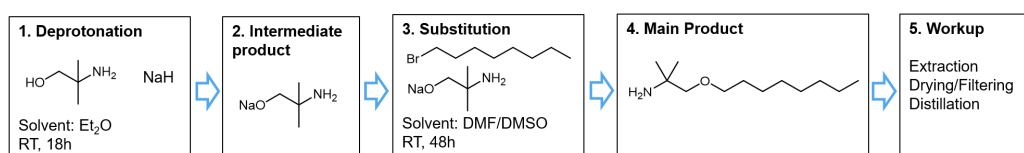


Figure 3: The various steps used for the synthesis of 2-methyl-1-(octyloxy)-2-propanamine (MOPA)

For the deprotonation step (part 1 in figure 3), 21.71 g (1.2 eq.) of 2-amino-2-methyl-1-propanol (AMP) was dissolved in a 250 mL round-bottom flask in approximately 100 mL of diethyl ether and slowly stirred under nitrogen atmosphere. 8.88 g (1.1 eq.) of sodium hydride as 40 wt. percent dispersion in mineral oil was washed twice. This was achieved by diluting the sodium hydride dispersion with approximately 40 mL of diethyl ether, centrifugation and removal of the solvent-oil mixture. This was performed twice, after which the sodium hydride was again diluted with diethyl ether and carefully added dropwise to the solution of AMP in the glass flask, during which bubbles evolved, indicating the formation of hydrogen gas. The reaction was stirred for 18 h at room temperature until no more bubbles evolved. This yielded the intermediate product (part 2 in figure 3). For the subsequent substitution step (part 3 in figure 3), the diethyl ether was then evaporated and the residues were diluted with 40 mL of a 50/50

mixture of DMF and DMSO. Then, 39 g (1.0 eq.) of 1-bromooctane (BRO) was added dropwise to the mixture. The reaction mixture was stirred for 48 h at room temperature under nitrogen atmosphere, resulting in the main product along with expected byproducts. *The workup* of the reaction was performed by liquid-liquid extraction using diethyl ether as the organic layer and distilled water as the aqueous layer. Multiple backwashes were performed to purify the organic layer. After the washing, the organic layer was dried with anhydrous magnesium sulfate and the solvent removed in the rotovap at a temperature of 60 °C and a pressure of 100 mbar until no more weight change was noticed. The weight of the raw product was 22.02 g. Since the raw product may also contain side products it was further purified by distillation. The pressure of the distillation setup was set to 40 mbar and the temperature of the oil bath was carefully increased until a steady condensation rate of distillate into the receiving flask was obtained. At this point, the temperature and pressure were held constant until no more distillate was collected, and the temperature reading for the vapour phase was noted. Only then, the receiving flask was exchanged for a new one, and the temperature again gradually increased in order to start collecting the next fraction. The purity of the obtained products was investigated using NMR spectroscopy using a 300 MHz spectrometer (Bruker, Germany).

3. Results and discussion

3.1. Fracture toughness and rheological properties

Fracture toughness. The results of the toughness measurements at room temperature and 77 K are summarized in table 3 and plotted in figure 4. The influence of different parameters (marked in blue) on the resulting properties was investigated. By comparing samples 1-3, a strong increase in the fracture toughness at cryogenic temperature is observed with increasing ratio R (decreasing crosslink density). An increase of the toughness is also observed when an excess of hardener is present in the system, reflected in the assumed functionality of the crosslinker, f. Lastly, the type of the chain extender also has a strong influence on the resulting toughness. All the systems containing alkylamines show a significantly improved fracture toughness over the base composition at cryogenic temperature. However, the effect is much smaller with the tert-octylamine and MOPA chain extender compared to the other alkylamines. In the case of tert-octylamine, its rigid molecular structure could affect its ability to form nanophase separated domains. However, it could also be that the strong sterical hindrance on the tert-octylamine could result a lesser degree of cure conversion and a weaker network. More surprisingly, the toughness of the MOPA system is also very low, despite having a flexible chain. These results will be further discussed in section 3.5, and a hypothesis established as to why the MOPA system shows a compromised toughness. At room temperature, all the samples exhibit low values of K_{Ic} , with only slight variations.

Rheological properties. Samples 5-8 were further characterized by rheological measurements. The results are shown in figure 5. Due to the volatility of the

Table 2: Sample overview, R is the molar ratio between DGEBA molecules and chain extender molecules. At $R = 1 : 0$, there are no chain extenders in the system, and each DGEBA molecule directly connects two crosslinker molecules. At $R = 1 : 1$, a theoretical case without crosslinker, DGEBA and chain extender molecules would form infinitely long chains, and thus a linear polymer. The variable f is the average functionality of the tetrafunctional hardener, based on the excess of hardener used. If no excess of hardener is used, $f = 4$. If an excess of hardener is used, some hardener molecules might not fully react, thus decreasing the average expected functionality, f . K_{Ic} is the plane strain fracture toughness, T_g the glass transition temperature and ρ the density.

System	ID	R	f	K_{Ic} (RT) MPa \sqrt{m}	K_{Ic} (LN2) MPa \sqrt{m}	T_g °C	ρ g/m ³
DGEBA, MPD	Base	1:0	4	0.8 ± 0.1	2.0 ± 0.1	178.8	1.217
DGEBA, BA, MPD	BA-4-5:4	5:4	4	1.2 ± 0.2	3.5 ± 0.6	75.9	1.153
DGEBA, BA, MPD	BA-4-9:8	9:8	4	1.5 ± 0.1	4.1 ± 0.6	67.6	1.145
DGEBA, BA, MPD	BA-2-9:8	9:8	2	1.9 ± 0.2	5.3 ± 0.4	70.0	1.145
DGEBA, BA , MPD	BA-3-9:8	9:8	3	1.6 ± 0.1	5.0 ± 1.1	72.6	1.147
DGEBA, OA , MPD	OA-3-9:8	9:8	3	1.8 ± 0.1	4.4 ± 0.5	54.1	1.109
DGEBA, t-OA , MPD	tOA-3-9:8	9:8	3	1.0 ± 0.1	2.7 ± 0.4	100.4	1.108
DGEBA, 2-HA , MPD	2HA-3-9:8	9:8	3	1.8 ± 0.1	4.7 ± 0.3	71.9	1.115
DGEBA, BA, MPD	BA-3-5:4	5:4	3	1.6 ± 0.2	4.7 ± 0.3	79.4	1.153
DGEBA, OA, MPD	OA-4-5:4	5:4	4	1.5 ± 0.2	4.6 ± 0.4	60.5	1.115
DGEBA, MOPA, MPD	MOPA-3-3:2	3:2	3	1.0 ± 0.7	1.62 ± 0.3	63.8	1.105

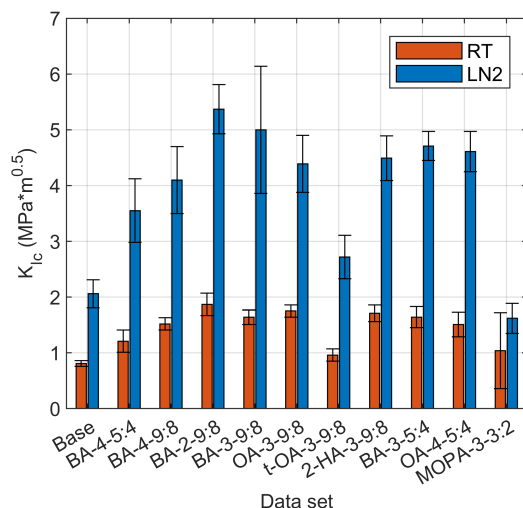


Figure 4: Values of the plane-strain fracture toughness at room temperature and at $-196\text{ }^{\circ}\text{C}$, measured for all samples.

difunctional amines and the resulting compositional change, no continuous measurement on the same sample was possible. To solve this problem, each sample was stored in a closed glass vial, and rheological measurements were performed at defined points in time using a new sample from the glass vial. For the systems containing simple n-alkylamines (butylamine, octylamine), the complex viscosity exceeds the processing-limit defined as 300 mPa s after 2 hours at a temperature of $22.5\text{ }^{\circ}\text{C}$ [2]. In contrast to this result, the viscosity increase of the systems containing substituents in β -position (tert-octylamine, 2-heptylamine) is much slower. Since the viscosity of the system is directly related to the degree of crosslinking, a lower reactivity of the substituted amines must be responsible for the extended pot-life. This supports our hypothesis that the sterical hindrance of the amine by the methyl groups attached on the β -position strongly reduces the reactivity, thereby increasing

the pot life. Due to these findings, MOPA (see figure 2), a molecule providing two methyl groups on the β -position and a significantly lower vapour pressure, was synthesized at the end of this study and also included in the mechanical tests.

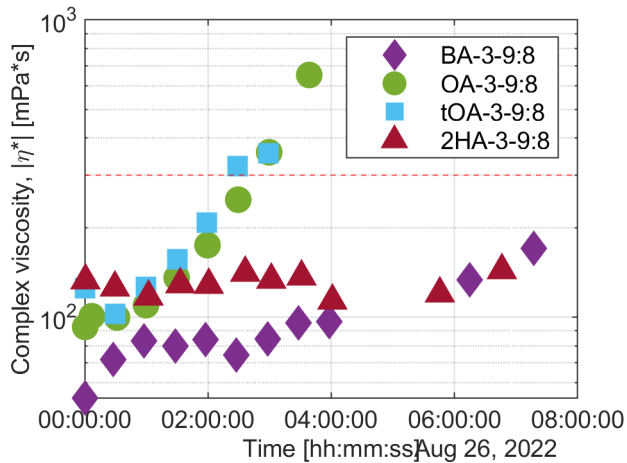


Figure 5: Time dependence of the complex viscosity of as-prepared mixtures stored at 22.5 °C for specified amounts of time. The measurements were done at 22.5 °C.

3.2. Wide angle x-ray scattering (WAXS)

The wide angle scattering pattern of the selected systems can be seen in figure 6. Each of the systems shows two strong distinct peaks, one at approximately 0.4 \AA^{-1} , the other at approximately 1.25 \AA^{-1} . According to the Bragg formula, these peaks correspond to distances in real space of about $2\pi/q = 15 \text{ \AA}$ and 5 \AA , respectively. The peak at 1.25 \AA^{-1} is the van-der-Waals peak found in almost all amorphous polymers [30]. The peak at the lower q-value could be caused by different phenomena. In the systems containing aliphatic side-chains a trend of decreasing peak position with in-

creasing length of the dangling chain is observed. However, the fact that this peak appears not only for the systems containing alkylamines, but can also be observed for the base system, strongly indicates that other causes than the hypothesized nanophase separation could be responsible for this peak. In fact, Dušek [30] also reports the occurrence of two distinct peaks in the WAXS spectra of very simple epoxy resin systems without side-chains, and even for amorphous polymers such as polystyrene or poly(methyl methacrylate). This shows that the proof for nanophase separation in the range of 0.5 – 2 nm is not a straightforward task, since scattering in this q-range could also originate from scattering from other repeating structures in the molecular network. The composition of the base system, which is shown in figure 6 was also investigated by Lovell and Windle [31]. Experimentally, they demonstrated that this peak only appears upon curing. Furthermore, the peak was found to be meridional, with the peak intensity increasing with increasing strain along the stretch direction in uniaxial tensile deformation. These findings strongly suggest that this peak must be related to the covalent network structure of the epoxy system. The appearance of the scattering peak at 0.4 \AA^{-1} was associated to type II chains in the epoxy network, more specifically, to the distances between the nitrogen atoms connected through crosslinked DGEBA molecules. Thus, it is evident that the occurrence of this peak alone is not sufficient to prove the existence of nanophase separation in epoxy-systems containing aliphatic side-chains.

Nano-scale phase-separation in polymers with chemically incompatible side-chains has been discussed from different perspectives. In multiple works [22, 23], a second peak was observed in poly(n-alkyl acrylates) apart from the

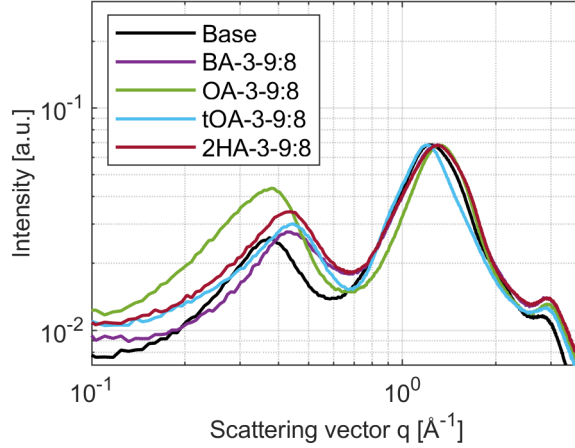


Figure 6: Wide angle x-ray scattering pattern of selected systems in arbitrary units. All the curves are scaled in so that the maxima of the second peak are at the same value.

van-der-Waals peak in the small-angle x-ray scattering (SAXS) curves, corresponding to a real space distance of approximately 15 Å. The corresponding Bragg distance of this peak was be in a linear correlation with the length of the side-chains and thus, the second peak was associated to nanodomains formed by the chemically incompatible side-chains.

3.3. Small angle x-ray scattering (SAXS)

The scattering profiles obtained by small angle scattering experiments can be seen in figure 7. Inhomogeneities in electron density on a larger scale than the postulated nanophase separation can be resolved using this technique. The peak at higher q -values corresponds to the polymerization peak discussed before. Interestingly, all the samples scatter strongly at low q -values, depicting power-law scattering, $I(q) \propto q^p$, with a power coefficient $p = -4$, which could be indicative of surface scattering of objects that are

larger than the wavelength of the scattered x-rays (Porod's law) [32]. The lowest q -values that were measured are at approximately 0.004 \AA^{-1} . This would correspond to a lower size limit of the surface-scattering structures of $2\pi/q = 157 \text{ nm}$. Thus, if there would be such entities, they could very likely be resolved using light microscopy, with the wavelengths of visible light ranging from approximately 680 nm down to 430 nm .

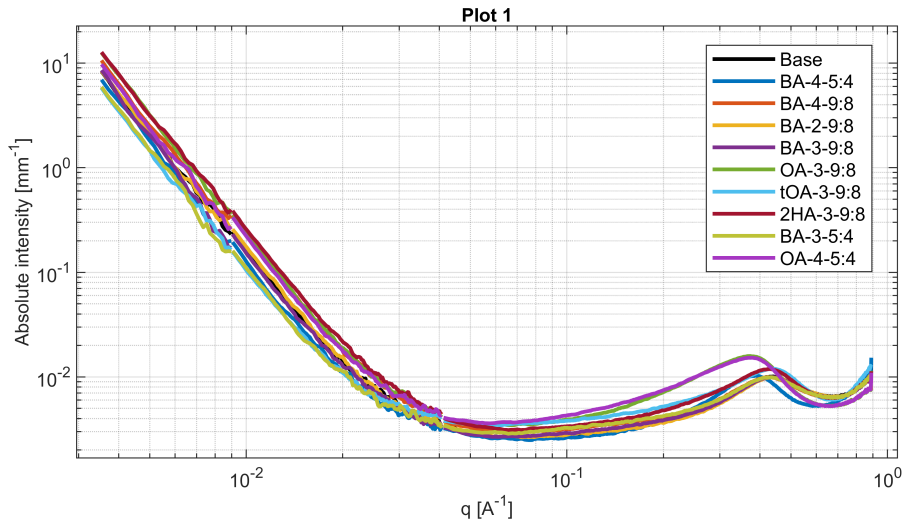


Figure 7: Small angle x-ray scattering profiles

3.4. DMTA

Figure 8 shows the dynamic mechanical properties of the investigated systems. At the glass transition temperature, the elastic modulus reduces by several orders of magnitude for all systems. The base system, which has the highest crosslink density, shows the smallest drop in elastic modulus and the highest elastic modulus in the rubbery regime. In the rubbery regime all the systems show a positive linear correlation between temperature and

elastic modulus, which is in agreement with rubber elasticity theory. Furthermore, the systems with a smaller expected crosslink density also show a lower elastic modulus in the rubbery regime. The only exception is the sample containing tert-octylamine, which exhibits a much lower modulus than similar samples. A possible explanation for this could be incomplete curing due to the sterically hindered amine groups. In the second plot in figure 8, the the loss tangent are plotted for the same systems. A broad β -relaxation peak at approximately -75°C is visible for all systems, including the base system. Sauvant and Halary [24] showed that phase-separating systems, such as phase-separating antiplasticizers, can be related to a β -relaxation peak. However, as the base system also depicts a broad β -relaxation peak, it is not possible to distinguish the relaxation peak due to phase separation from a β -relaxation that is common to all epoxy systems used in this study.

In the lower temperature range below the glass transition temperature, all the elastic moduli approach very similar values, which agrees with the findings of other authors [2]. However, there still is a variation of elastic moduli. They are found to be very well correlated with the density of the investigated systems, as can be seen in figure 9. This finding can be rationalized using Grüneisens first rule for isotropic van-der-Waals materials, which states that the elastic modulus at 0 K is related to the cohesive energy density, E_{coh} , and the molar volume, V_{0K} , as [33]:

$$E_{0K} = 3(1 - 2\nu)\frac{mn}{4} \frac{E_{\text{coh}}}{V_{0K}} \quad (8)$$

The base system containing only DGEBA and MPD has the highest storage modulus, and it also has no olefinic side-chains. The amount of olefinic side-

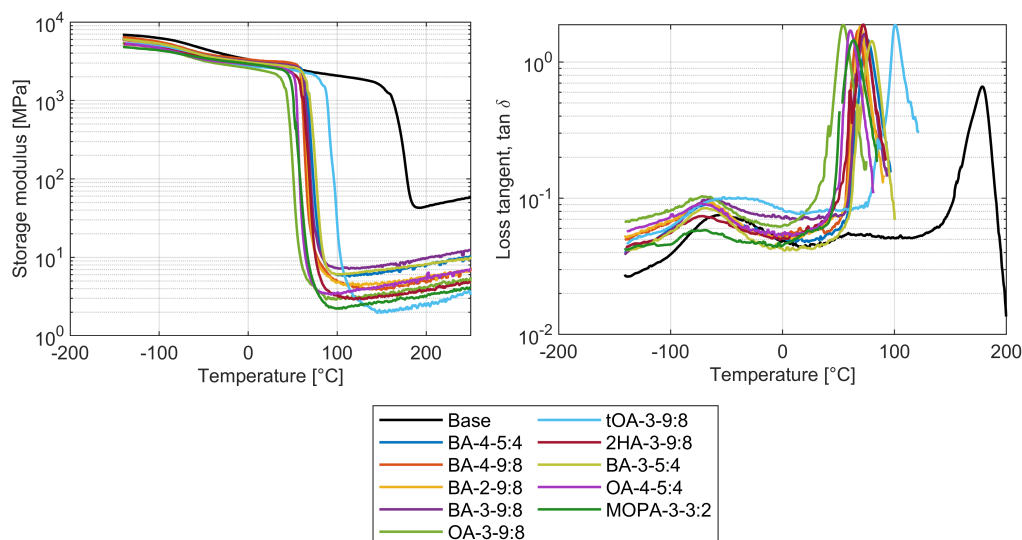


Figure 8: The storage modulus E' as a function of temperature (left plot) shows a decrease of multiple orders of magnitude as the glass transition is reached. The plot on the right side shows the corresponding peaks of the loss tangent, which were used to determine the glass transition temperatures of the systems.

chains is correlated with the density (as polyethylene has a lower density than polycarbonate, for example) as well as the cohesive energy density (as olefinic side-chains cannot interact with higher energy such as hydrogen bonding).

3.5. Tensile Tests and Crosslink Density

Tensile tests performed above T_g , in order to obtain reliable estimates for the crosslink density according to equation 5. The nominal stress versus nominal strain curves for each experiment are presented in figure 10. The tests were performed at nominal strains not exceeding 2% in order to avoid rupture of the samples. This also ensures a practically linear behaviour

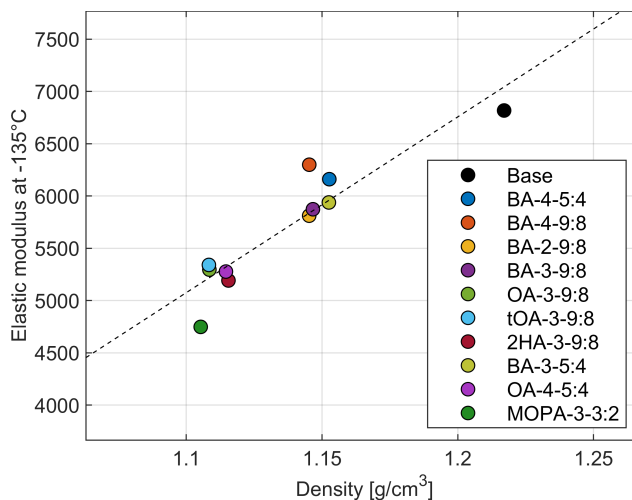


Figure 9: Elastic modulus at -135°C (below the β -relaxation) plotted versus the measured density

useful for the analysis of the crosslink density. As can be seen in figure 10, the stress-strain curves are linear and the moduli increase with increasing temperatures. Usually the samples started to turn darker in color during the last temperature step performed at 230°C , indicating the beginning of thermal degradation in the epoxy material.

Figure 10 shows the elastic moduli extracted at different temperatures plotted for each sample. For all the samples, the elastic modulus gradually increased with increasing temperature, pointing out entropic-elastic behaviour. The extracted moduli were then linearly fitted, and the slope, representing $\partial E'/\partial T$, was used to obtain estimates for the crosslink density according to 5.

In figure 12 and 12, the toughness values are plotted versus the measured crosslink density at 77K and room temperature, respectively. Both plots show similar trends, and are therefore discussed together. In general, for

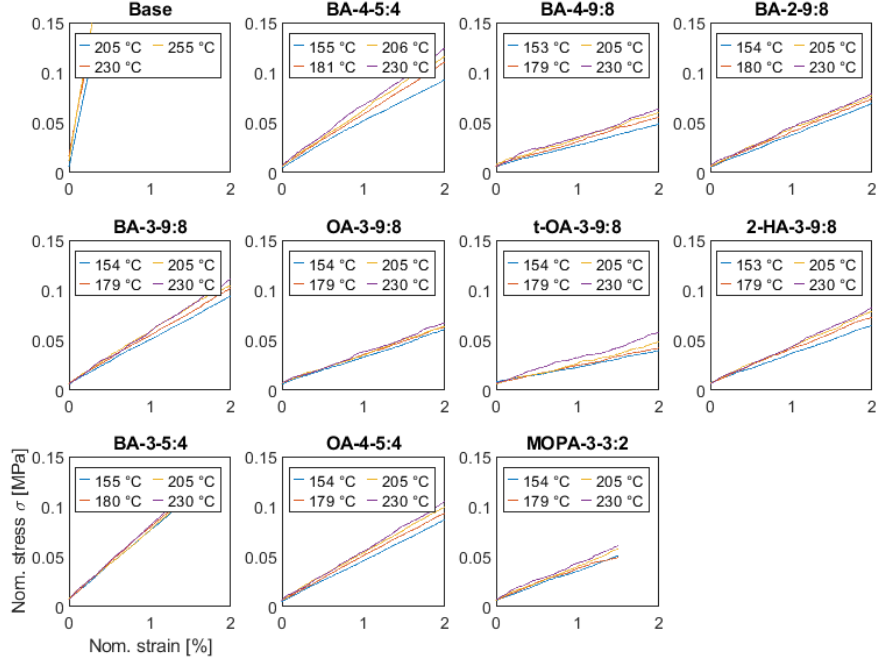


Figure 10: Stress-strain curves measured in uniaxial tensile deformation at Temperatures above the glass transition of the respective systems.

most of the samples, a trend of sharply increasing toughness with decreasing crosslink density is observed. Two outliers with low values of K_{Ic} were observed, for the systems **tOA-3-9:8** and **MOPA-3-3:2**. In figure 14, the crosslink density measured from $\partial E' / \partial T$ is plotted versus the crosslink density estimates obtained from equation 6. The dashed line marks the theoretical line where the predicted crosslink density equals the measured one. For the **tOA-3-9:8** system, the plot shows that the measured crosslink density is even a bit higher than the predicted crosslink density. This means that the crosslink density is not compromised, and that the system has been properly cured. Thus, we think that the low fracture toughness of this system

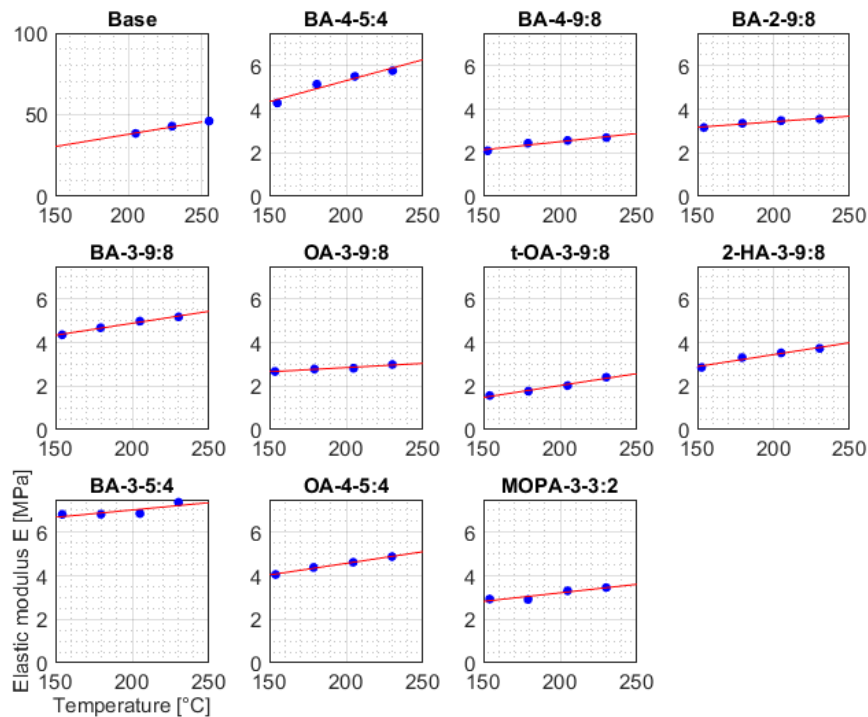


Figure 11: The blue data points represent the elastic moduli obtained by linear fits of the data obtained in the uniaxial tensile deformation experiments (see fig. 10). These data points were subsequently linearly fitted, and the so obtained slope ($\partial E'/\partial T$) was used to determine the crosslink density according to equation 5.

must be rooted in the conformational rigidity of the tert-octylamine molecule compared to the other molecules flexible dangling chains. For some systems, especially the **MOPA-3-3:2** system, the measured crosslink density is much smaller than the predicted one. From this we conclude that this system is not fully crosslinked, despite having been cured under the same conditions and the same extent of sterical hindrance by methyl groups. We hypothesize here that this finding is due to network topological reasons, in that the

configuration composed of rather long side chains dilutes the system to such an extent that it is unable to find a conformation of the network that allows the reaction of all the crosslinks.

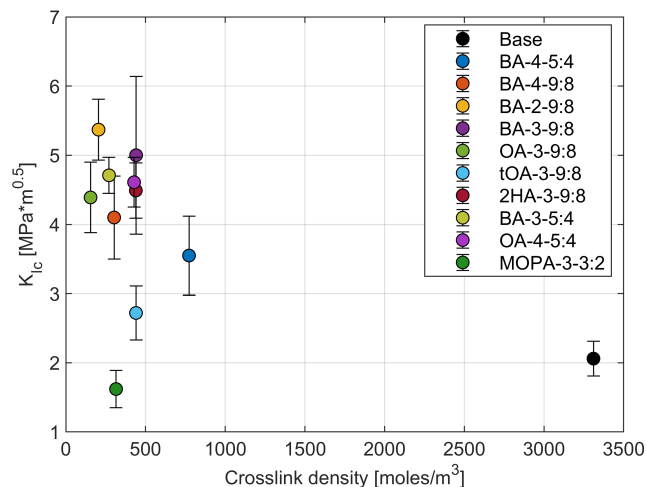


Figure 12: The measured values of the fracture toughness at a temperature of $-196\text{ }^{\circ}\text{C}$ plotted versus the crosslink derived from tensile tests data and equation 5.

3.6. Chain extender synthesis

Three separate fractions were collected during distillation at a reduced pressure of 40 mbar. The first fraction weighed 1.24 g and was collected at a vapour phase temperature of $32\text{ }^{\circ}\text{C}$. The second fraction weighed 18.53 g and was collected at a temperature of $133\text{ }^{\circ}\text{C}$. The third fraction weighed 2.25 g and was collected at temperatures exceeding $150\text{ }^{\circ}\text{C}$. The first two fractions were clear and low viscous liquids, whereas the third fraction was a very dark coloured and viscous liquid. The H-NMR of the second fraction is shown in figure 15. The observed resonance peaks, as well as their relative integral values, correspond very well to what would be expected for the product.

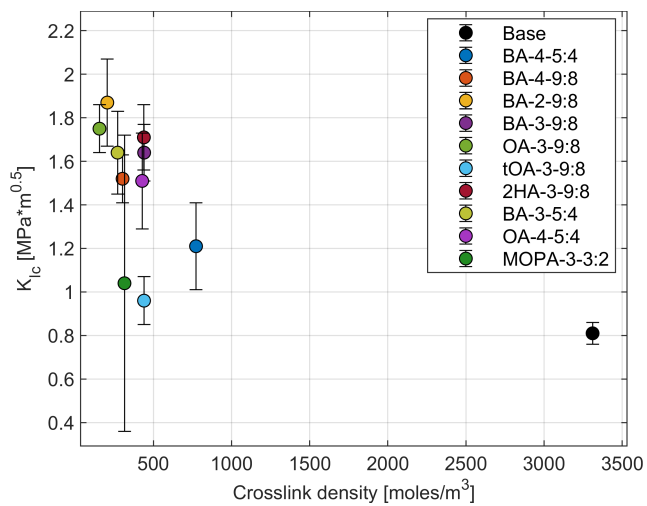


Figure 13: The measured values of the fracture toughness at a temperature of 25 °C plotted versus the crosslink derived from tensile tests data and equation 5.

Thus, we successfully synthesized the desired compound. The yield was 45.6%. The peaks and their assignments are compiled in table 3.

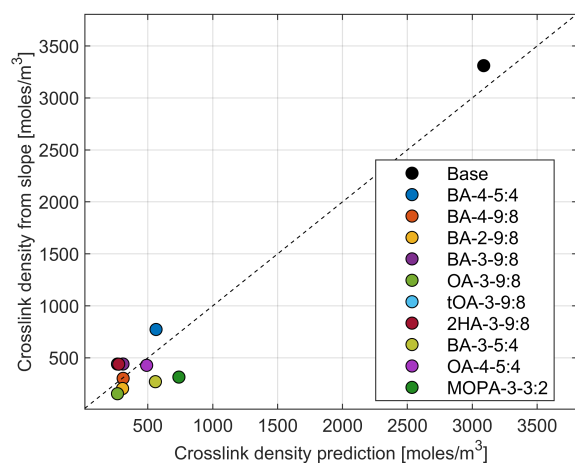


Figure 14: Values of the crosslink density derived from the slope $\partial E'/\partial T$ plotted versus crosslink density predictions from equation 6.

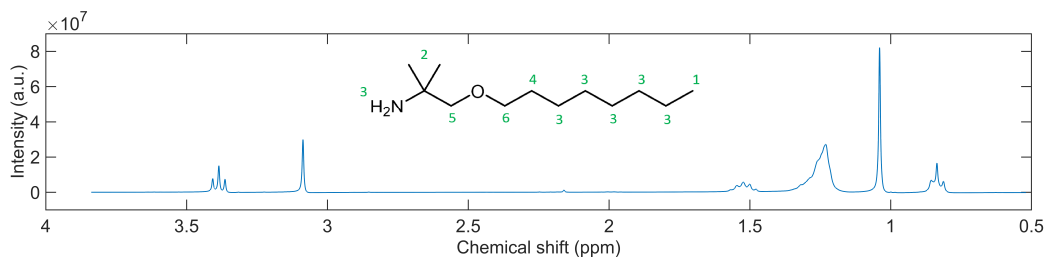


Figure 15: Proton NMR spectrum of the synthesized compound dissolved in CDCl₃

Table 3: This table shows the assignments of the various peaks of the H-NMR spectrum shown in figure 15.

Peak shift (ppm)	Assignment	Expected Int.	Measured Int.
0.84	-CH ₃ (t)	1.50	1.45
1.04	2 -CH ₃ (s)	3.00	2.94
1.23	5 -CH ₂ -, -NH ₂	6.00	6.33
1.52	-CH ₂ - (q)	1.00	1.16
3.09	-CH ₂ - (s)	1.00	1.00
3.39	-CH ₂ - (t)	1.00	1.05

4. Conclusion and outlook

From the results we conclude that the incorporation of flexible olefinic side-chains into epoxy networks can significantly improve the fracture toughness of epoxy resins at cryogenic temperatures. We tried to confirm our hypothesis of nanophase separation by DMTA and scattering methods. In the scattering experiments, the q -range for which scattering in case of nanophase separation was expected, was overlapping with the q -range of scattering from the network structure. Likewise, in the DMTA measurements, additional relaxation peaks expected in case of nano-phase separation could be distinguished from commonly occurring β -relaxations in epoxy systems. Thus, nano-phase separation could not be confirmed experimentally but could also not be excluded. The rheological measurements revealed a significant improvement of processing lifetime of the resin when a sterically hindered amine, such as 2-aminoheptane, was used as an olefinic chain extender. By this approach, we found a new epoxy resin formulation which is very well suited for cryogenic applications. This formulation provides a long processable lifetime and low viscosity, a high toughness at 77 K and glass transition well above temperature, providing mechanical stability at room temperature for handling of coil assemblies. We also successfully synthesized another chain extender providing a much lower vapour pressure, which would thus be more suitable for VPI processes. It was hypothesized that the bad performance of this chain extender in an epoxy system was due to topological constraints given by the network parameters, and thus it would be interesting to test a similar chain extender, but with a smaller length of the alkyl chain, in order to increase the Ratio R. Additionally, the thermal expansion mismatches be-

tween the epoxy insulation and the superconducting wires and other parts of the coil also play an important role. As was shown by Brem et al. [2], the thermal expansion coefficients is similar for all epoxy resins at low temperatures, and thus an additional phase needs to be introduced into the epoxy resin for modification of thermal expansion. The mismatch could be reduced by introducing hard, ceramic nanoparticles into an epoxy matrix, which may simultaneously increase the toughness.

Appendix A. My Appendix

Appendix sections are coded under `\appendix`.

`\printcredits` command is used after appendix sections to list author credit taxonomy contribution roles tagged using `\credit` in frontmatter.

References

- [1] D. Evans, Resins for Superconducting Magnet Construction - An Overview of Requirements, Processing and Properties, IOP Conference Series: Materials Science and Engineering 756 (2020). doi:10.1088/1757-899X/756/1/012003.
- [2] A. Brem, B. J. Gold, B. Auchmann, D. Tommasini, T. A. Tervoort, Elasticity, plasticity and fracture toughness at ambient and cryogenic temperatures of epoxy systems used for the impregnation of high-field superconducting magnets, Cryogenics 115 (2021). doi:10.1016/j.cryogenics.2021.103260.

- [3] Z. Sápi, R. Butler, Properties of cryogenic and low temperature composite materials – A review, *Cryogenics* 111 (2020) 103190. URL: <https://doi.org/10.1016/j.cryogenics.2020.103190>. doi:10.1016/j.cryogenics.2020.103190.
- [4] T. H. Hsieh, A. J. Kinloch, K. Masania, A. C. Taylor, S. Sprenger, The mechanisms and mechanics of the toughening of epoxy polymers modified with silica nanoparticles, *Polymer* 51 (2010) 6284–6294. URL: <http://dx.doi.org/10.1016/j.polymer.2010.10.048>. doi:10.1016/j.polymer.2010.10.048.
- [5] B. C. Kim, S. W. Park, D. G. Lee, Fracture toughness of the nanoparticle reinforced epoxy composite, *Composite Structures* 86 (2008) 69–77. doi:10.1016/j.compstruct.2008.03.005.
- [6] B. B. Johnsen, A. J. Kinloch, R. D. Mohammed, A. C. Taylor, S. Sprenger, Toughening mechanisms of nanoparticle-modified epoxy polymers, *Polymer* 48 (2007) 530–541. doi:10.1016/j.polymer.2006.11.038.
- [7] W. Chang, L. R. Rose, M. S. Islam, S. Wu, S. Peng, F. Huang, A. J. Kinloch, C. H. Wang, Strengthening and toughening epoxy polymer at cryogenic temperature using cupric oxide nanorods, *Composites Science and Technology* 208 (2021) 108762. URL: <https://doi.org/10.1016/j.compscitech.2021.108762>. doi:10.1016/j.compscitech.2021.108762.
- [8] B. Zhang, W. Wang, M. Tian, N. Ning, L. Zhang, Prepa-

- ration of aramid nanofiber and its application in polymer reinforcement: A review, *European Polymer Journal* 139 (2020) 109996. URL: <https://doi.org/10.1016/j.eurpolymj.2020.109996>. doi:10.1016/j.eurpolymj.2020.109996.
- [9] J. Jung, H. A. Sodano, High strength epoxy nanocomposites reinforced by epoxy functionalized aramid nanofibers, *Polymer* 195 (2020) 122438. URL: <https://doi.org/10.1016/j.polymer.2020.122438>. doi:10.1016/j.polymer.2020.122438.
- [10] E. Ahmadloo, A. A. Gharehaghaji, M. Latifi, H. Saghafi, N. Mohammadi, Effect of PA66 nanofiber yarn on tensile fracture toughness of reinforced epoxy nanocomposite, *Proceedings of the Institution of Mechanical Engineers, Part C: Journal of Mechanical Engineering Science* 233 (2019) 2033–2043. doi:10.1177/0954406218781910.
- [11] S. F. Teh, T. Liu, L. Wang, C. He, Fracture behaviour of poly(ethylene terephthalate) fiber toughened epoxy composites, *Composites Part A: Applied Science and Manufacturing* 36 (2005) 1167–1173. doi:10.1016/j.compositesa.2004.08.007.
- [12] L. Daelemans, O. Verschate, L. Heirman, W. Van Paepegem, K. De Clerck, Toughening mechanisms responsible for excellent crack resistance in thermoplastic nanofiber reinforced epoxies through in-situ optical and scanning electron microscopy, *Composites Science and Technology* 201 (2021) 108504. URL: <https://doi.org/10.1016/j.compscitech.2020.108504>. doi:10.1016/j.compscitech.2020.108504.

- [13] W. L. Bradley, W. Schultz, C. Corleto, S. Komatsu, The Synergistic Effect of Cross-Link Density and Rubber Additions on the Fracture Toughness of Polymers (1993) 317–334. doi:10.1021/ba-1993-0233.ch013.
- [14] R. J. Varley, Toughening of epoxy resin systems using low-viscosity additives 84 (2004) 78–84. doi:10.1002/pi.1321.
- [15] J. H. Hodgkin, G. P. Simon, R. J. Varley, Thermoplastic toughening of epoxy resins: A critical review, *Polymers for Advanced Technologies* 9 (1998) 3–10. doi:10.1002/(SICI)1099-1581(199801)9:1;3::AID-PAT727;3.0.CO;2-I.
- [16] U. Farooq, J. Teuwen, C. Dransfeld, Toughening of epoxy systems with interpenetrating polymer network (IPN): A review, *Polymers* 12 (2020). doi:10.3390/POLYM12091908.
- [17] M. Sharifi, C. W. Jang, C. F. Abrams, G. R. Palmese, Toughened epoxy polymers via rearrangement of network topology, *Journal of Materials Chemistry A* 2 (2014) 16071–16082. doi:10.1039/c4ta03051f.
- [18] N. Tian, R. Ning, J. Kong, Self-toughening of epoxy resin through controlling topology of cross-linked networks, *Polymer* 99 (2016) 376–385. URL: <http://dx.doi.org/10.1016/j.polymer.2016.07.038>. doi:10.1016/j.polymer.2016.07.038.
- [19] M. Bakar, J. Szymanska, J. Rudecka, J. Fitas, Effect of reactive diluents and kaolin on the mechanical properties of epoxy resin, *Polymers and Polymer Composites* 18 (2010) 503–510. doi:10.1177/096739111001800905.

- [20] A. Zubeldia, M. Larrañaga, P. Remiro, I. Mondragon, Fracture toughening of epoxy matrices with blends of resins of different molecular weights and other modifiers, *Journal of Polymer Science, Part B: Polymer Physics* 42 (2004) 3920–3933. doi:10.1002/polb.10675.
- [21] E. Crawford, A. J. Lesser, The effect of network architecture on the thermal and mechanical behavior of epoxy resins, *Journal of Polymer Science, Part B: Polymer Physics* 36 (1998) 1371–1382. doi:10.1002/(SICI)1099-0488(199806)36:8<1371::AID-POLB11>3.0.CO;2-4.
- [22] M. Beiner, H. Huth, Nanophase separation and hindered glass transition in side-chain polymers, *Nature Materials* 2 (2003) 595–599. doi:10.1038/nmat966.
- [23] S. Hiller, O. Pascui, H. Budde, O. Kabisch, D. Reichert, M. Beiner, Nanophase separation in side chain polymers: New evidence from structure and dynamics, *New Journal of Physics* 6 (2004). doi:10.1088/1367-2630/6/1/010.
- [24] V. Sauvant, J. L. Halary, Novel formulations of high-performance epoxy-amine networks based on the use of nanoscale phase-separated antiplasticizers, *Journal of Applied Polymer Science* 82 (2001) 759–774. doi:10.1002/app.1902.
- [25] Y. Huang, Y. Tian, Y. Li, X. Tan, Q. Li, J. Cheng, J. Zhang, High mechanical properties of epoxy networks with dangling chains and tunable

- microphase separation structure, *RSC Advances* 7 (2017) 49074–49082. doi:10.1039/c7ra08886h.
- [26] A. S. Mora, R. Tayouo, B. Boutevin, G. David, S. Caillol, A perspective approach on the amine reactivity and the hydrogen bonds effect on epoxy-amine systems, *European Polymer Journal* 123 (2020) 109460. URL: <https://doi.org/10.1016/j.eurpolymj.2019.109460>. doi:10.1016/j.eurpolymj.2019.109460.
- [27] P. J. Flory, Molecular theory of rubber elasticity, *Polymer* 20 (1979) 1317–1320.
- [28] M. Shen, M. Croucher, Contribution of Internal Energy to the Elasticity of Rubberlike Materials, *Journal of Macromolecular Science, Part C* 12 (1975) 287–329. doi:10.1080/15321797508076109.
- [29] B. R. Pauw, Erratum: Everything SAXS: Small-angle scattering pattern collection and correction (*Journal of Physics Condensed Matter* (2013) 25 (383201)), *Journal of Physics Condensed Matter* 26 (2014). doi:10.1088/0953-8984/26/23/239501.
- [30] K. Dušek, Are cured thermoset resins inhomogeneous?, *Angewandte Makromolekulare Chemie* 240 (1996) 1–15. doi:10.1002/apmc.1996.052400101.
- [31] R. Lovell, A. H. Windle, WAXS investigation of local structure in epoxy networks, *Polymer* 31 (1990) 593–601. doi:10.1016/0032-3861(90)90274-3.

- [32] G. Beaucage, Approximations Leading to a Unified Exponential/Power-Law Approach to Small-Angle Scattering, *Journal of Applied Crystallography* 28 (1995) 717–728. doi:10.1107/s0021889895005292.
- [33] M. G. Broadhurst, Bulk Modulus and Grüneisen Parameters for Linear Polymers, *The Journal of Chemical Physics* 52 (1970) 3634. doi:10.1063/1.1673537.